Chemical Science

ROYAL SOCIETY OF CHEMISTRY

EDGE ARTICLE

View Article Online
View Journal

Cite this: DOI: 10.1039/d6sc03686d

All publication charges for this article have been paid for by the Royal Society of Chemistry

Upcycling of $LiFePO_4$ to high-performance $LiMn_xFe_{1-x}PO_4$: activating the Mn redox platform for stable energy storage

Zihao Zeng,† Xuepeng Qi,† Wei Sun, Peng Ge and Yue Yang *

Received 1st May 2026
Accepted 26th May 2026

DOI: 10.1039/d6sc03686d

rsc.li/chemical-science

Driven by the demand for greener and cost-effective solutions for lithium-ion battery recycling, direct regeneration of cathode materials from spent batteries has gained significant attention. To address the growing requirements for higher operating voltage and energy density in energy storage systems, $LiMn_xFe_{1-x}PO_4$ (LMFP) has emerged as a promising cathode material for next-generation batteries due to its superior electrochemical performance compared to conventional $LiFePO_4$ (LFP). Herein, we propose a novel upcycling strategy that transforms LFP into high-performance LMFP through a facile high-temperature solid-state synthesis method. The regenerated LMFP cathode exhibits reduced particle size, well-defined crystallinity, and exceptional electrochemical properties, delivering a specific capacity of 144.7 mAh g^{-1} at 0.5C, a rate capability of 120.5 mAh g^{-1} at 5.0C, and 91.1% capacity retention after 500 cycles at 1.0C. The underlying phase transformation and Mn activation mechanisms during high-temperature calcination were systematically investigated, revealing critical insights into the structural evolution from LFP to LMFP. This work provides fundamental insights into the design of efficient upcycling strategies for transitioning low-voltage cathodes to advanced high-energy-density materials, offering both environmental and technological benefits for sustainable energy storage.

Introduction

Lithium-ion batteries (LIBs) have been widely applied in portable devices, energy storage, electric vehicles, *etc.*[1–4] Lithium-ion batteries (LIBs) based on lithium iron phosphate (LFP) cathodes have attracted attention due to their stable structure, long cycle life, and high safety.[5–7] However, with the booming of LFP batteries, a large amount of spent LFP will inevitably be generated.[8,9] It is estimated that the cumulative capacity of spent LFP batteries will reach 147.1 GWh by 2030. These spent batteries contain both hazardous components and large amounts of valuable components such as lithium (Li), phosphorus (P), and iron (Fe).[10,11] If they are not properly disposed of, it can lead to serious environmental problems and waste of valuable resources.[12–14] To solve the above problems, a series of recycling technologies have been proposed, including the pyrometallurgical method, hydrometallurgical method, and direct regeneration.[15–17] The pyrometallurgical method requires a lot of energy to reach the required melting temperature, resulting in high carbon emissions. The hydrometallurgical method consumes a large amount of acid/alkali to leach and separate valuable metals. It not only involves a long process but also produces a lot of wastewater and waste salt, facing the problems of high cost and serious secondary pollution.[14,16,18,19] Compared with pyrometallurgical and hydrometallurgical methods, direct regeneration repairs components and defects of spent LFP materials to restore their electrochemical performances without separation and extraction of valuable elements.[20] For instance, utilizing a multifunctional organic lithium salt (3,4-dihydroxybenzonitrile di-lithium, Li_2DHBN), the degraded LFP cathode materials can be directly restored by Zhou's group, displaying good cycling stability and rate performance (a high capacity retention of 88% after 400 cycles at 5C).[21] By tailoring oxidation–reduction manners, Zeng *et al.* successfully achieved the reconfiguration of the spent LFP lattice and prepared uniform cathode regeneration materials, displaying excellent electrochemical performance at 2.0C with a capacity of 137 mAh g^{-1} and a retention rate of 92% after 300 cycles.[22] Because of its low emission of pollutants and short process for preparing high-value-added products, direct regeneration has been considered as one of the most promising methods for spent LFP recycling.

However, at present, LFP suffers from low energy density caused by its low potential of ~3.4 V, which makes it unable to meet the pursuit of high energy density in the electric vehicle industry.[23,24] Meanwhile, the lithium manganese iron phosphate ($LiMn_xFe_{1-x}PO_4$, $0 < x < 1$; abbreviated as LMFP) material has developed rapidly. This material has a similar stable olivine structure to the LFP material, so it has the same safety as LFP. At

School of Minerals Processing and Bioengineering, Central South University, Changsha 410083, China. E-mail: yangyue18@csu.edu.cn; Eric1911@126.com

† These authors contributed equally to this work and should be regarded as co-first authors.

the same time, the introduction of manganese (Mn) elevated the overall electrode potential of the battery cathode material (the standard electrode potential: $E_{Mn^{2+}/Mn^{3+}}$ (1.542 V) > $E_{Fe^{2+}/Fe^{3+}}$ (0.771 V)), and the electrochemical platforms for the material can be increased to 4.5 V, giving it an energy density comparable to that of ternary materials. Therefore, it is known as a high-performance cathode for next-generation power batteries.[25–29]

At present, LMFP is mainly synthesized by the solvothermal method, the coprecipitation method, and the high-energy ball-milling (HEBM)-assisted solid-state reaction method,[27,29] which have the problems of long processes and high cost. Considering that LFP and LMFP materials have similar results, if the composition, structure, and morphology characteristics of spent LFP can be fully utilized, appropriate manganese sources can be introduced, and manganese is uniformly distributed in the crystal lattice through controllable element migration, it is possible to regeneratively prepare LMFP materials and realize the upgraded utilization of spent LFP.[30] Inspired by this, we propose a simple and efficient solid-state synthesis method for $LiMn_{0.4}Fe_{0.6}PO_4/C$ by utilizing a pure LFP phase and manganese salts. Unlike common synthesis methods, our process fully disperses the material in the fluid by adding an ethanol solution at the high-energy ball milling stage, which increases the contact interface between the particles and promotes solid-

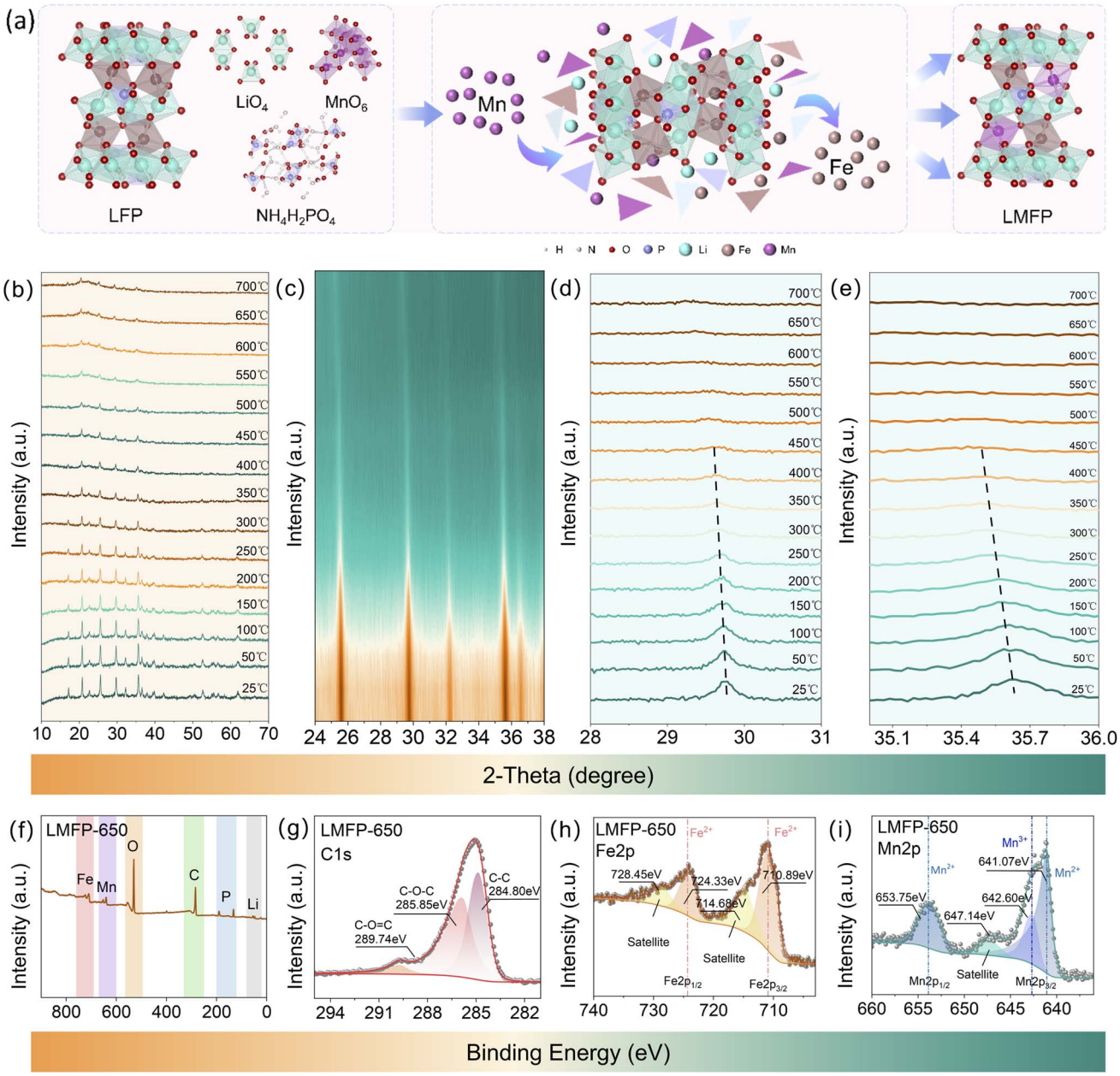

Fig. 1 (a) Schematic illustration of the proposed mechanism of structural recombination. (b–e) The *in situ* XRD results of the samples at high temperatures. (f) The full XPS spectrum of as-prepared LMFP-650. The high-resolution XPS spectra of (g) Fe 2p, (h) Mn 2p, and (i) C 1s of LMFP-650.

phase reactions. The LFP particles used in the raw material can provide the precursor with a stable crystal framework structure, which is conducive to the dissolution and diffusion of Mn into the crystal lattice under high temperature conditions, thus resulting in a solid solution with uniform distributions of Fe and Mn. Detailed characterization studies revealed the structural information of regenerated LFMP. As expected, the upcycled LMFP material delivered excellent electrochemical performance (initial capacity of 144.7 mAh g^{-1} at 0.5C and 91.1% capacity retention after 500 cycles at 1C). Compared with the traditional recycling methods, our proposed direct upcycling strategy is environmentally friendly and economically feasible, and thus can provide some references for the direct recycling and upgrading of waste LFP into new LMFP cathode materials.

Results and discussion

First, the reaction mechanism of regenerating LMFP was revealed by *in situ* XRD, as shown in Fig. 1a. Precursors are evenly mixed by ball milling and then calcined and annealed under an argon atmosphere. Fig. 1b–e exhibit the *in situ* X-ray diffraction (XRD) pattern of regenerated LMFP during calcination. At room temperature (25 °C), the material exhibits the characteristic peaks of the LFP phase. As the temperature increases, the (211) and (311) crystal peaks shift to smaller angles due to the lattice expansion triggered by the entry of Mn into LFP crystals to replace the Fe sites (the radius of Mn^{2+} (0.83 Å) is larger than that of Fe^{2+} (0.63 Å)).[22,31] Furthermore, the peak shifts are continuous, indicating that the Mn substitution occurring in the Fe region belongs to the solid-solution phase transformations rather than a two-phase reaction from the LFP phase to the LMFP phase.[32–34] When the temperature exceeds 450 °C, only the characteristic peaks of LMFP can be observed. To further explore the calcination conditions, the structures of samples with different calcination cut-off temperatures above 400 °C (650 °C, 700 °C, 750 °C, and 800 °C, named LMFP-650, LMFP-700, LMFP-750, and LMFP-800, respectively) were tested.[22,31,35,36]

It is well known that valence changes can be determined with high sensitivity by X-ray photoelectron spectroscopy (XPS) analysis; thus, the investigation on the XPS spectra of as-prepared samples is conducted in Fig. 1f–i. Fig. 1f displays the complete XPS spectrum of the selected sample LMFP-650, where distinct peaks for Li, P, C, Mn, and Fe can be noted. Fig. 1g presents the XPS spectrum of Fe 2p for LMFP-650. The characteristic peaks at 710.89 and 724.33 eV were attributed to the divalent states Fe $2p_{3/2}$ and Fe $2p_{1/2}$, and two shoulder peaks at 714.68 and 728.45 eV.[22,37,38] Similarly, in the XPS spectrum of Mn 2p of LMFP-650 (Fig. 1h), it can be observed that the Mn peaks are separated into two parts due to spin inductive coupling, and the characteristic peaks at the binding energies of 641.07 and 653.75 eV are attributed to the divalent state.[23,38–41] The peak at a binding energy of 642.60 eV indicates that the sample particles may have generated a small fraction of Mn^{3+} during sintering, which may undergo a disproportionation reaction, leading to the instability of the cell in the earliest few cycles. Furthermore, the presence of carbon layers can be revealed by the XPS spectra of C 1s of LMFP-650 (Fig. 1i). The peak located at 284.80 eV is related to the C–C bonds, the peak at 285.85 eV is related to the formation of the C–O–C bonds, and the peak at 289.74 eV can be attributed to the C–O═C bonds.[22,38] According to the results above, the reaction mechanism of the synthesis process can be summarized in Fig. 1a. Under the action of ball milling, the LFP powder is thoroughly mixed with the Mn salt and glucose to form precursors. At high temperatures, glucose generates a series of molecules with strong reducing ability, ensuring that the added Mn salt produces Mn^{2+}, which gradually enters the LFP crystals and displaces Fe^{2+} to form the LMFP solid solution. In addition, in spite of the glucose, there are still some unreacted Mn salts produced as Mn^{3+} due to oxidation, which has a certain effect on the electrochemical performance of the material. Subsequently, after high-temperature carbonization, the doped glucose will eventually be wrapped in the outer layer of LMFP particles in the form of disordered carbon, forming a conductive matrix and improving the rate-capability during the charge–discharge process. The commercial LFP starting material contains a small amount of residual carbon from its original synthesis. During upcycling, glucose-derived carbon forms a new conductive layer on the particle surface. Thus, the final carbon coating is a hybrid of the residual carbon and the glucose-derived carbon, which together enhance electronic conductivity.

XRD patterns of LMFP-650, LMFP-700, LMFP-750, and LMFP-800 are shown in Fig. S2 (SI). It can be seen that all samples show similarly strong diffraction peak features that match well with the standard PDF cards of $LiFePO_4$ (JCPDs: 81-1173) and $LiMnPO_4$ (JCPDs: 74-0375), with no impurity peaks detected. The position of the (311) characteristic peaks (Fig. S3, SI) shown by the enlarged diffraction pattern in the 2-Theta

Table 1 Molar mass and ratio of elements in the samples

	Sintering temperature							
	650 °C		700 °C		750 °C		800 °C	
Elements	Molar mass/mol	Ratio	Molar mass/mol	Ratio	Molar mass/mol	Ratio	Molar mass/mol	Ratio
Li	0.6369	**1.0493**	0.6297	**1.0486**	0.6556	**1.1037**	0.6254	**1.0585**
Fe	0.3456	**0.5694**	0.3402	**0.5666**	0.3492	**0.5878**	0.3402	**0.5759**
Mn	0.2439	**0.4019**	0.2366	**0.3941**	0.2457	**0.4137**	0.2366	**0.4005**
P	0.6070	**1.0000**	0.6005	**1.0000**	0.5940	**1.0000**	0.5908	**1.0000**

interval from 34.5° to 36.0° is shifted compared to the LFP particles.[42] According to Bragg's law ($n\lambda = 2d\sin\theta$), when the lattice spacing (d) increases, the Bragg's angle (θ) decreases, so when the characteristic peaks of Fe sites in the crystal are shifted backward, it indicates that Mn has partially replaced Fe, which triggers the expansion of the lattice and the formation of the olivine structure of the LMFP phase. The exact chemical composition of the upgraded LMFP materials was determined by ICP-OES, and the results are shown in Table 1 and Fig. S1 (SI). The ratios of Li, Fe, Mn, and P in the four samples were found to converge to 1.0 : 0.6 : 0.4 : 1.0, which closely matched the expected values of $LiMn_{0.4}Fe_{0.6}PO_4$.[21]

As is known, the morphological properties served a crucial role in Li^+-storage performance. First, scanning electron microscopy (SEM) and transmission electron microscopy (TEM) were conducted here to investigate the structure of the samples LMFP-650, LMFP-700, LMFP-750, and LMFP-800. It can be seen in the SEM images exhibited in Fig. 2a1–a4 that the size of the material particles shows an increasing trend as the sintering temperature increases. LMFP-650 contains slightly more small-sized particles than LMFP-700 and LMFP-750, while LMFP-800 exhibits severe agglomeration. The smaller particle size nanocrystals not only provide a larger specific surface area to help electrolyte penetration and provide more paths for lithium ion diffusion, but also shorten the lithium ion and electron hopping paths and accelerate the embedding/de-embedding process of lithium ions, which contributes to higher multiplication performance.[22,23] In the TEM images (Fig. 2c and d)

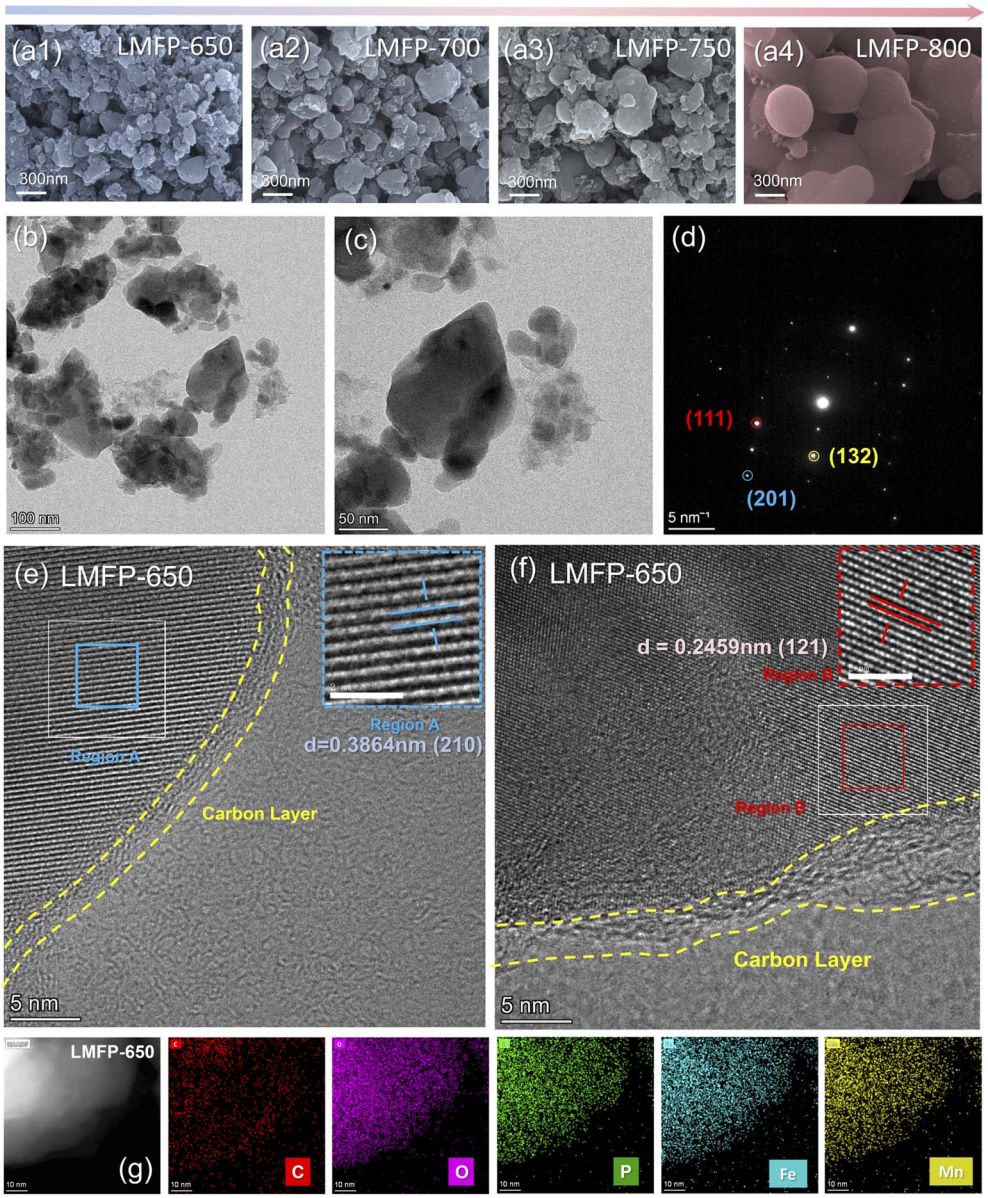

Fig. 2 The SEM images of (a1) LMFP-650, (a2) LMFP-700, (a3) LMFP-750 and (a4) LMFP-800. For the LMFP-650 material: (b) TEM images, (c) enlarged TEM images, (d) selected area diffraction pattern, (e and f) high-resolution TEM images, and (g) EDS elemental mapping.

showing the internal structure of the sample particles, we can observe that the LMFP-650 particles are connected by a free carbon film, showing irregular morphology and varying particle size. The high-resolution TEM (HR-TEM) images (Fig. 2e and f) demonstrate the clear lattice fringes and thin carbon layer on the surface of the sample particles. Supported by the analysis of the Gatan Digital Micrograph, the lattice distance corresponding to different crystal planes of LFP-500 could be determined. 0.3864 nm is assigned to the (210) crystal plane, and 0.2459 nm is assigned to the (121) plane. The coated carbon layer derived from glucose and the carbon film wrapped around the particles together construct a three-dimensional electronically conductive carbon network, which can effectively enhance the conductivity of the material and make up for the defects of LMFP as an electrode material, which is an insulator itself.[43] The Fast-Fourier-Transform (FFT) pattern of LMFP-650 (Fig. 2d) shows the image of a single crystal with obvious diffraction spots, indicating that it is well crystallized. In addition, the

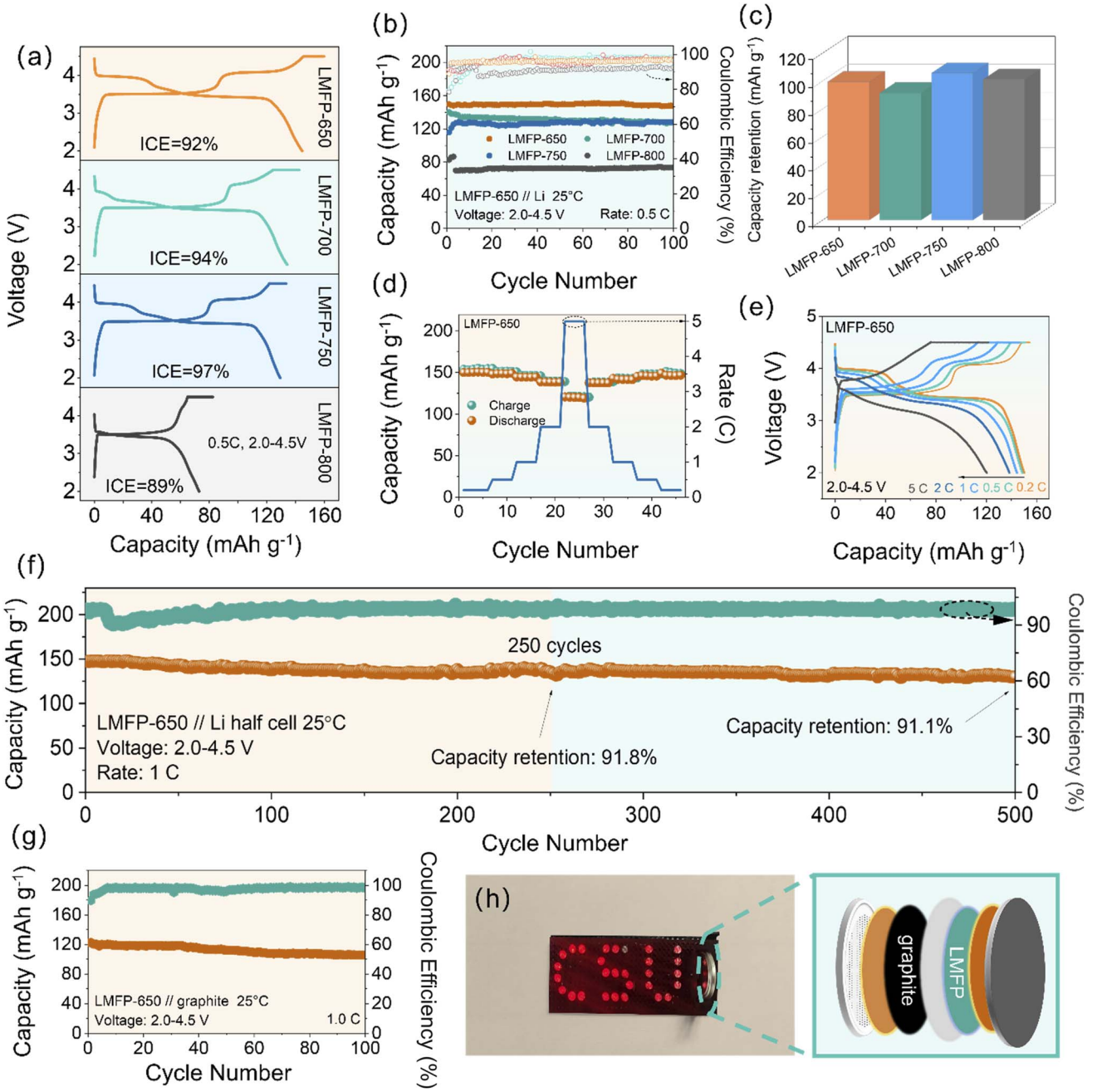

Fig. 3 (a) The charging/discharging curves of LMFP-650/700/750/800 at 0.5C. (b) Cycling performance of LMFP-650 at 0.5C. (c) The cycling performance of LMFP-650/700/750/800 at 0.5C. (d) The rate performance of LMFP-650 at different current densities. (e) The charging/discharging curves of LMFP-650 at different current densities. (f) Cycling performance of LMFP-650 at 1.0C. (g) Electrochemical performance of the LMFP-650//graphite full cell. (h) The images of LEDs designed with the "CSU" pattern powered by the LMFP-650//graphite full cell.

energy dispersive spectroscopy (EDS) elemental maps of LMFP/C (Fig. 2g) show that all the elements are uniformly distributed without any aggregation. The above results well demonstrate the morphology design of the LMFP/C composite crystal material.

The above compositional and structural analyses indicate that the LMFP prepared by LFP upgrading has the potential to exhibit excellent electrochemical properties. Firstly, their charge–discharge curves were measured at 0.5C (1.0C = 170 mAh g^{-1}) in the voltage range from 2.0–4.5 V (*vs.* Li^+/Li) (Fig. 3a). Unlike LFP, the LMFP/C will present two voltage plateaus synchronized at about 3.5 and 4.0 V, which correspond to the oxidation reactions of Fe^{2+}/Fe^{3+} and Mn^{2+}/Mn^{3+}, respectively. Compared to pure $LiFePO_4$ ($\approx$3.4 V) and $LiMnPO_4$ ($\approx$4.1 V), the discharge plateaus for Fe^{2+}/Fe^{3+} and Mn^{2+}/Mn^{3+} in LMFP-650/700/750 materials display slight differences, which are mainly caused by the ion super-exchange effect of transition metals in the LMFP solid solution and voltage decay due to mismatch strain in the crystal upon Li^+ embedding/de-embedding.[32,42,44,45] In addition, it can be clearly seen that the Mn^{2+}/Mn^{3+} charging/discharging platform of the LMFP-800 material almost disappears, and its specific capacity decreases dramatically, which indicates that too high a calcination temperature will have an unfavorable effect on the performance of the electrode material. The discharge specific capacities for LMFP-650, LMFP-700, LMFP-750, and LMFP-800 materials are 144.7, 134.2, 129.3, and 72.9 mAh g^{-1}, respectively, at a charge/discharge rate of 0.5C. The capacity retention rates after 100 cycles (Fig. 3b and c) are 98.71%, 93.02%, 99.03%, and 99.89%, which show basic cycling stability. The high specific capacity of LMFP-650 shows that a smaller particle size and appropriate carbon content can lead to excellent electrochemical performance. It is well known

Table 2 The electrochemical properties of LMFP samples in previous work and this work

Samples	Synthesis method	Capacity [mAh g^{-1}, C]	Capacity retention	Reference
$LiMn_{0.5}Fe_{0.5}PO_4$ (MF55)	A solid-state synthesis method by utilizing $LiFePO_4$ and nano $LiMn_{0.7}Fe_{0.3}PO_4$	142.3 mAh g^{-1} at 0.5C	91.2% after 300 cycles at 0.5C	31
$LiMn_{0.25}Fe_{0.75}PO_4$ (R-LMFP-G12)	A direct upcycling scheme for leached $FePO_4$ material toward LMFP material	161.3 mAh g^{-1} at 0.1C	98.8% after 300 cycles at 1C	42
$LiMn_{0.5}Fe_{0.5}PO_4$	A simple hydrothermal process followed	145.7 mAh g^{-1} at 0.5C	84.6% after 100 cycles at 5C	50
$LiMn_{0.5}Fe_{0.5}PO_4$	Composites *via* a facile and versatile electrospinning strategy	150 mAh g^{-1} at 0.2C	119% after 500 cycles at 0.2C	38
$LiMn_{0.8}Fe_{0.2}PO_4$	A modified spray drying process	140 mAh g^{-1} at 0.2C	90.2% after 200 cycles at 0.2C	51
$LiMn_{0.9}Fe_{0.1}PO_4$	A mechano-chemical activation assisted high temperature carbon thermal reduction method	144 mAh g^{-1} at 0.5C	100% after 100 cycles at 2C	52
$LiMn_{0.5}Fe_{0.5}PO_4$	A microwave-assisted hydrothermal synthesis in pure water	160 mAh g^{-1} at 0.5C	87% after 1000 cycles at 1C	47
$LiMn_{0.5}Fe_{0.5}PO_4$	A mechanical activation-assisted method by utilizing spent $LiFePO_4$ and $LiMn_2O_4$	143.9 mAh g^{-1} at 0.5C	98.47% after 100 cycles at 1C	53
$LiFe_{0.6}Mn_{0.4}PO_4$	Sintering spherical precursor powders prepared by a modified spray drying method	145 mAh g^{-1} at 0.5C	98.9% after 100 cycles at 2C	54
$LiMn_{0.5}Fe_{0.5}PO_4$	A solid-phase synthesis	135 mAh g^{-1} at 0.5C	—	33
$LiFe_{0.8}Mn_{0.2}PO_4$	A novel sol–gel hydrothermal method	134.8 mAh g^{-1} at 0.2C	97.46% after 100 cycles at 0.2C	28
$LiMn_{0.5}Fe_{0.5}PO_4$	Rheological phase reaction with stearic acid as the carbon source	105 mAh g^{-1} at 0.5C	95% after 300 cycles at 1C	55
$LiMn_{0.6}Fe_{0.4}PO_4$	Composed of [001]-oriented nanorods and assembled into dense microspheres	156.8 mAh g^{-1} at 0.5C	97.8% after 300 cycles at 1C	56
$LiMn_{0.5}Fe_{0.5}PO_4$	A facile solution-based synthesis route	147 mAh g^{-1} at 1C	97% after 100 cycles at 1C	57
$LiMn_{0.4}Fe_{0.6}PO_4$	A simple solid-phase synthesis strategy based on the rheological phase reaction	144.7 mAh g^{-1} at 0.5C	91.1% after 500 cycles at 1C	This work

that the long-cycle capacity of cathode materials plays a key role in large-scale energy storage applications, and thus the capacity and cycling stability of LMFP-650 were measured at a current density of 1.0C in Fig. 3f. Although LMFP-650 exhibits an attractive capacity (142.7 mAh g^{-1}), it shows capacity decay after 500 cycles, which is attributed to the Jahn–Teller effect of the Mn-containing material.[34]

Fig. 3d illustrates the rate performance of LMFP-650 at different current densities, and its discharge specific capacities at 0.2C, 0.5C, 1.0C, 2.0C, and 5.0C are 150.3, 148.7, 144.5, 138.4, and 120.5 mAh g^{-1}, respectively. On the plots of the charge/discharge curves at different multiplicities shown in Fig. 3e, it is noteworthy that an additional plateau is observed at high C-rates, and the plateau corresponding to the Mn^{2+}/Mn^{3+} reaction disappears in the voltage profile. Previous studies have suggested that the former is due to the kinetic limitation of the electrochemical reactions,[32,45] and the latter is related to the generation of the intermediate phase L_xMFP and the specific phase transition behavior of the LMFP material during charging and discharging at high C-rates.[32,34,46–49] The extra plateau originates from the Fe^{2+}/Fe^{3+} reaction but is altered due to the presence of Mn in the lattice. In a homogeneous $LiMn_{0.4}Fe_{0.6}PO_4$ solid solution, the Fe and Mn ions are randomly distributed on transition-metal sites. At low rates, Fe and Mn react sequentially. However, the Fe-rich region would delithiate first at ~3.5 V, followed by Fe sites occupied by Mn at 3.0–3.5 V, resulting in the formation of an additional platform. Furthermore, the additional platform could be further aggravated by the small particle size of LMFP-650 (noted in Fig. 2a1), which is beneficial for rate capability but also promotes the formation of the extra platform. For further evaluating the application potential of LMFP-650, an LMFP-650//graphite full-cell was assembled, as shown in Fig. 3h, which delivered 120 mAh g^{-1} at 1.0C and exhibited attractive electrochemical stability (Fig. 3g and h). By comparison with previous work (Table 2) focused on the preparation of LMFP cathode materials, the LMFP/C composites upgraded from LFP, especially LMFP-650, showed better electrochemical properties, including specific capacity and cycling stability, proving that the present work is of some reference significance for the preparation of LMFP electrode materials.

Thereafter, in order to refine the study of Li^+ diffusion kinetics in LMFP/C, we performed cyclic voltammetry (CV) tests at different scan rates (0.1, 0.3, 0.5, 0.7, and 0.9 mV s^{-1}) in the

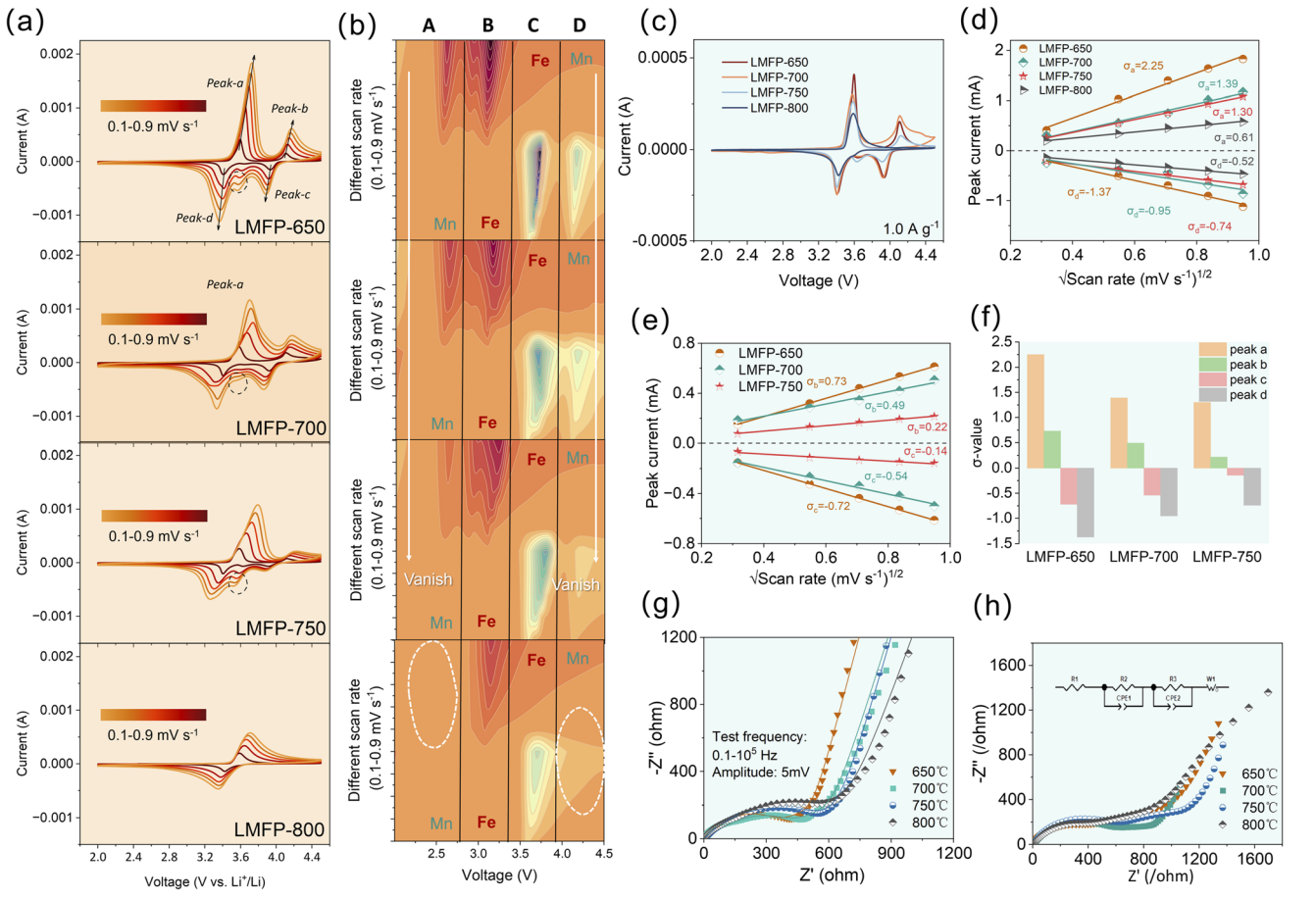

Fig. 4 (a) The CV curves at different scan rates of LMFP-650, LMFP-700, LMFP-750, and LMFP-800. (b) Counter maps of CV curves at different scan rates of LMFP-650, LMFP-700, LMFP-750, and LMFP-800. (c) The first CV curves of LMFP-650, LMFP-700, LMFP-750, and LMFP-800 at 0.1 mV s^{-1}. Linear relationships between scan rates and peak currents of (d) Fe and (e) Mn. (f) Comparison of the values of the four peaks. The pristine Nyquist plots of samples during (g) the first cycle and (h) the 20th cycle.

range of 2.0–4.5 V (Fig. 4a). The oxidation and reduction peaks observed in the CV curves are the same as the platforms in the charge–discharge curves described above, and the CV curves at different scan rates have similar shapes, indicating that the as-prepared LMFP materials have good electrochemical reversibility. In all the samples, the oxidation peaks move towards higher voltage and the reduction peaks move towards lower voltage as the scan rate increases, indicating that the higher the scan rate, the greater the polarization. Furthermore, counter maps of different CV curves revealed the Mn platform vanishing behaviors in Fig. 4b. With the increase in sintering temperature, Mn peaks vanished in region A and region D, and Fe peaks in regions B and C remained at their original intensities. It could be concluded that Mn-dominated energy storage capability receded at high sintering temperatures (>650 °C); thus, 650 °C served as the most suitable temperature for the upcycling of spent LFP. The suppression of the Mn^{2+}/Mn^{3+} plateau at 700 °C can be attributed to several factors. Firstly, elevated sintering temperatures promote the disproportionation of Mn^{3+} into Mn^{2+} and Mn^{4+}, as evidenced by the XPS detection of minor Mn^{3+} in LMFP-650 (Fig. 1h). The resulting Mn^{4+} is inactive in the olivine structure, reducing the number of reversible Mn^{2+}/Mn^{3+} redox centers. Secondly, Mn segregation toward grain boundaries or particle surfaces may occur at higher temperatures, forming inactive phases that further diminish the Mn^{2+}/Mn^{3+} activity. Fig. 4c compares the first CV curve of the four samples. Compared to LMFP-700/750/800, LFP-650 displayed lower over-potential. To probe the inner reason for the Mn vanishing behavior, we plot in Fig. 4d–f the matched linear fit curves between the peak current density (I_p) and the square root of the scan rate ($v^{1/2}$) to calculate the apparent ion diffusion coefficient (D_{Li}) according to the Randles–Sevcik equation:[21,58]

$$I_p = (2.65 \times 10^5) n^{3/2} S D_{Li}^{1/2} C_{Li} v^{1/2}$$

where I_p, n, S, D_{Li}, C_{Li}, and v are the peak current, number of electrons, area of the electrode, Li-ion diffusion coefficient, Li-ion concentration in the electrode, and voltage sweep rate, respectively. D_{Li} is positively correlated with the slope of the $I_p/v^{1/2}$ curve. Therefore, at the same Li-ion concentration, the larger the slope of the curve, the higher the ion diffusion coefficient and the faster the Li^+ migration rate in this region. For all the samples, the value of the Li^+ diffusion coefficient (Li–Fe) corresponding to the Fe redox region is higher than the corresponding value for Mn (Li–Mn), which indicates that the

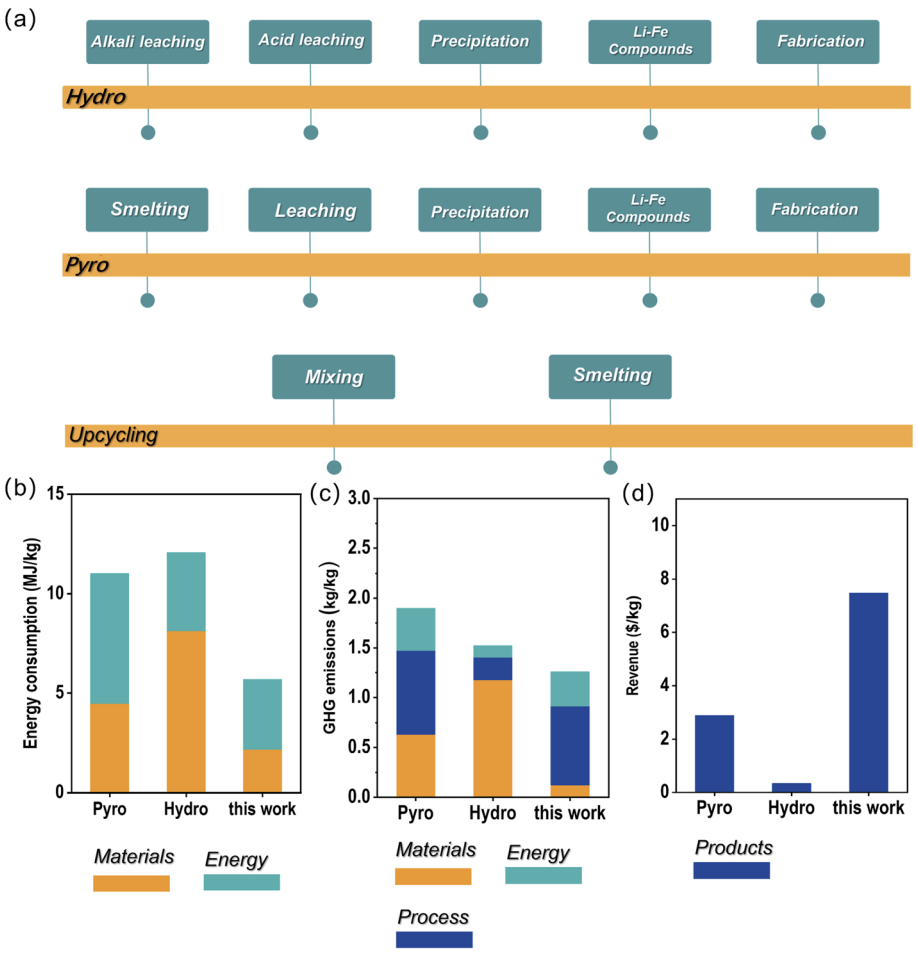

Fig. 5 (a) Regeneration steps of the pyrometallurgical recovery process (Pyro), hydrometallurgical process (Hydro), and upcycling strategy. (b) Energy consumption, (c) greenhouse gas emissions, and (d) economic benefits of the three recycling methods.

migration rate of Li^+ is faster in the Fe region than in the Mn region. The Jahn–Teller effect of Mn^{3+} induces local lattice distortions, leading to slower kinetic behavior during the Mn^{3+}/Mn^{2+} redox reaction.[23]

The electrochemical impedance spectra (EIS) of Fig. 4g demonstrate the change in internal resistance during the first cycle for each of the four samples, and the pristine Nyquist curves in the plots all consist of a small intercept in the high-frequency region (ohmic resistance R_s), a semicircle in the high mid-frequency regions (charge transfer resistance at the electrode/electrolyte solution interface, R_{ct}), and a diagonal line in the low-frequency region (Warburg impedance W_0).[22,42] Based on the ZVIEW software and equivalent circuit model, the R_{ct} values can be calculated and are 409.1, 462.6, 541.1, and 564.7 Ω in that order as the temperature increases. LMFP-650 has the smallest R_{ct} value and the highest slope line in the low-frequency region, indicating the fastest Li-ion diffusion rate. Subsequently, we also performed a secondary test on a battery with 20 cycles of charge/discharge cycling, which shows in Fig. 4h an increase in the resistance at the electrode/electrolyte interface. This is related to the microstructural changes caused by the embedded detachment of lithium ions and the thickening of the solid electrolyte interface (SEI) on the electrode surface.[34,59] LMFP-650 exhibits the best electrochemical performance by having the largest intrinsic Li-ion diffusion coefficient, the fastest Li-ion migration rate, the smallest R_{ct} value, the largest slope of the straight line, and the smallest Li^+ and charge transfer impedance.

So far, a series of strategies have been proposed to recycle waste LFP cathode materials, such as the pyrometallurgical recovery process (Pyro) and hydrometallurgical process (Hydro). In this work, an upcycling process was proposed to convert LFP to LMFP with high energy density. To evaluate the economic and environmental value of the upcycling process, the related analysis was conducted as follows.[60] Herein, several key assumptions are made for a fair comparison, which can be found in the SI. The functional unit is 1 kg of spent LFP black mass, and full details are in the SI (Tables S1–S4). Compared to the pyrometallurgical recovery process (Pyro) and the hydrometallurgical process (Hydro), the upcycling process shows the advantages of a simple operation process (Fig. 5a). Furthermore, the upcycling process displayed attractive economic and environmental value. As shown in Fig. 5b and c, compared to the pyrometallurgical recovery process (Pyro) and hydrometallurgical process (Hydro), the upcycling process in this work possessed lower energy consumption and GHG emissions, demonstrating considerable environmental value. Importantly, the upcycling process in this work could achieve higher revenue than the traditional process (Fig. 5d), contributing to the commercial promotion of the upcycling strategy.

Conclusion

In this report, a simple high-temperature solid-phase synthesis strategy was proposed to effectively upgrade the pure LFP phase into LMFP cathode materials. In the wet ball milling process, high-energy ball milling reduces the particle size of the added raw material, and the flowing ethanol solution mixes the material uniformly to form the precursor. During the elevated temperature sintering process, the added Mn gradually occupies the Fe sites in LFP in the form of a solid solution phase transition, forming elementally homogeneous and structurally complete LMFP crystals. The structural morphology exploration and electrochemical properties of the samples synthesized at different final firing temperatures showed that the LMFP-650 material synthesized at a final firing temperature of 650 °C has a smaller particle size, optimal capacity, multiplicity, and cycling performance. Specifically, the discharge specific capacity reaches 144.7 mAh g^{-1} at 0.5C multiplicity and retains 91.1% of its initial capacity after 500 cycles at 1C. Although this study focuses on the synthesis of LMFP with a Mn/Fe ratio of 2 : 3, the scheme involved in this work can be applied to produce LMFP materials with other Mn/Fe ratios (*e.g.*, 1 : 1). Therefore, the approach in this work is informative for the direct regeneration and upgrading of waste LFP into new LMFP cathode materials.

Experimental section

Materials preparation

Herein, pure LFP was purchased from Taiwan Likai Company, anhydrous alcohol was purchased from a chemical company in Hunan, China, and all other raw materials were purchased from the Macklin Company. Coin cell battery components were also purchased from Guangdong Canrd New Energy Technology Co., Ltd, including coin cells, Celgard 2500 separator, polyvinylidene fluoride (PVDF), carbon black, aluminum (Al) foil, and Li metal discs. The electrolyte was purchased from DoDochem, which was composed of $LiPF_6$ (1 M), ethylene carbonate (EC), diethyl carbonate (DEC), and dimethyl carbonate (DMC) (EC : DEC : DMC = 1 : 1 : 1 vol%).

LMFP cathode material preparation

First, pure LFP particles were ball-milled for 2 h at 400 rpm, after which the anhydrous alcohol, $[Mn(CH_3COO)_2]\cdot 4H_2O$, $LiOH\cdot H_2O$, and $NH_4H_2PO_4$ were added and milling was continued for 4 h, and finally glucose pellets were added and milled for another 4 h. The ground precursors were dried at 80 °C to remove the alcohol. Later, the dried samples were preheated at 350 °C for 3 h and further reheated at 650 °C for 10 h to obtain the LMFP samples. Four different final firing temperatures of 650, 700, 750, and 800 °C, named LMFP-650, LMFP-700, LMFP-750, and LMFP-800, were selected to explore the optimal sintering conditions for the process.

Materials characterization

Through *in situ* XRD, the reaction mechanism could be probed. For determining the composition and valence states of the LMFP samples, X-ray photoelectron spectroscopy (Thermo Fischer, ESCALAB Xi+) was used for XPS testing. An inductively coupled plasma emission spectrometer (ICP) was used to investigate the element content. X-ray diffraction (XRD) analysis was performed to identify the composition of the as-prepared

material. The morphology and architecture of the LMFP materials were explored by scanning electron microscopy (SEM) and transmission electron microscopy (TEM).

Electrochemical characterization

For the assembly of half cells, prepared LMFP was used as the active material, and CR2016-type half coin cells were assembled in an argon-filled glovebox. In the cells, the counter electrode was lithium metal, and the electrolyte was 1 M $LiMn_2O_4/LiPF_6$ in ethylene carbonate/diethyl carbonate/dimethyl carbonate (EC : DMC : DEC = 1 : 1 : 1). The Celgard 2500 membrane was used as the separator. Active materials (prepared LMFP), polyvinylidene difluoride (PVDF), and conductive carbon black particles (conductive agent, radius of 30 nm) were blended to obtain the slurry (active materials : conductive carbon black : PVDF binder = 80 : 10 : 10 wt%). Then, the slurry was evenly distributed on the Al foil to prepare working electrodes. For the assembly of full cells, the anode was replaced by graphite. Correspondingly, active materials (graphite), carboxymethyl cellulose (CMC, binder), and conductive carbon black particles (conductive agent, radius of 30 nm) were blended to prepare the slurry (active materials : conductive carbon black : CMC binder = 95 wt% : 2 wt% : 3 wt%). In this work, the LMFP cathode sheets contained about ~0.5 mg of LMFP samples. Herein, a battery cycler (CT3001A) was used to investigate the galvanostatic charge and discharge tests, rate performances, and electrochemical behaviors of the prepared LMFP. Meanwhile, cyclic voltammetry (CV) testing and electrochemical impedance spectroscopy (EIS) testing were conducted on a Solartron Analytical instrument.

Author contributions

Z. Z. and X. Q. contributed to investigation and writing of original draft. W. S. and P. G. contributed to review and editing. Y. Y. contributed to conceptualization, writing of original draft, and review and editing. All authors discussed the results and commented on the manuscript.

Conflicts of interest

There are no conflicts to declare.

Data availability

The data supporting this article have been included as part of the supplementary information (SI). Supplementary information: detailed structural information of regenerated LMFP materials and detailed data for economic analysis. The figures (Fig. S1–S3) display molar ratio and XRD patterns of LMFP. The tables (Tables S1–S4) provide the data sources, materials price, and energy prices of economic analysis. See DOI: https://doi.org/10.1039/d6sc03686d.

Acknowledgements

This work was financially supported by the State Key Program of the Major Research Plan of the National Natural Science Foundation of China (No. 92575204) and the Sichuan Science and Technology Program (2025ZDZX0080).

References

1 E. Fan, L. Li, Z. Wang, J. Lin, Y. Huang, Y. Yao, R. Chen and F. Wu, *Chem. Rev.*, 2020, **120**, 7020–7063.
2 H. E. Melin, M. A. Rajaeifar, A. Y. Ku, A. Kendall, G. Harper and O. Heidrich, *Science*, 2021, **373**, 384–387.
3 M. Wang, K. Liu, S. Dutta, D. S. Alessi, J. Rinklebe, Y. S. Ok and D. C. W. Tsang, *Renew. Sustain. Energy Rev.*, 2022, **163**, 112515.
4 N. Nitta, F. Wu, J. T. Lee and G. Yushin, *Mater. Today*, 2015, **18**, 252–264.
5 Y. Wang, P. He and H. Zhou, *Energy Environ. Sci.*, 2011, **4**, 805–817.
6 Y. Xu, B. Zhang, Z. Ge, S. Zhang, B. Song, Y. Tian, W. Deng, G. Zou, H. Hou and X. Ji, *J. Cleaner Prod.*, 2024, **434**, 140077.
7 J. Liu, Z. Bao, Y. Cui, E. J. Dufek, J. B. Goodenough, P. Khalifah, Q. Li, B. Y. Liaw, P. Liu, A. Manthiram, Y. S. Meng, V. R. Subramanian, M. F. Toney, V. V. Viswanathan, M. S. Whittingham, J. Xiao, W. Xu, J. Yang, X.-Q. Yang and J.-G. Zhang, *Nat. Energy*, 2019, **4**, 180–186.
8 Y. Tao, C. D. Rahn, L. A. Archer and F. You, *Sci. Adv.*, 2021, **7**, eabi7633.
9 G. Harper, R. Sommerville, E. Kendrick, L. Driscoll, P. Slater, R. Stolkin, A. Walton, P. Christensen, O. Heidrich, S. Lambert, A. Abbott, K. Ryder, L. Gaines and P. Anderson, *Nature*, 2019, **575**, 75–86.
10 J. Zhang, Z. Dong, Z. Zeng, Y. Zhao, W. Sun, P. Ge and Y. Yang, *Adv. Funct. Mater.*, 2026, **36**, e22632.
11 P. Ge, X. Lu, Z. Zeng, C. Zhu, H. Lei, W. Sun and Y. Yang, *Adv. Funct. Mater.*, 2026, **36**, e74810.
12 B. Gangaja, S. Nair and D. Santhanagopalan, *ACS Sustainable Chem. Eng.*, 2021, **9**, 4711–4721.
13 Y. Lan, X. Li, G. Zhou, W. Yao, H. Cheng and Y. Tang, *Adv. Sci.*, 2024, **11**, 2304425.
14 Y. Yang, S. Song, S. Lei, W. Sun, H. Hou, F. Jiang, X. Ji, W. Zhao and Y. Hu, *Waste Manage.*, 2019, **85**, 529–537.
15 T. Yang, D. Luo, A. Yu and Z. Chen, *Adv. Mater.*, 2023, **35**, 2203218.
16 P. Zhu, Z. Jiang, W. Sun, Y. Yang, D. S. Silvester, H. Hou, C. E. Banks, J. Hu and X. Ji, *Energy Environ. Sci.*, 2023, **16**, 3564–3575.
17 G. Ji, D. Tang, J. Wang, Z. Liang, H. Ji, J. Ma, Z. Zhuang, S. Liu, G. Zhou and H.-M. Cheng, *Nat. Commun.*, 2024, **15**, 4086.
18 J. Zhou, X. Zhou, W. Yu, Z. Shang, Y. Yang and S. Xu, *Nano Energy*, 2024, **120**, 109145.
19 G. Qian, Z. Li, Y. Wang, X. Xie, Y. He, J. Li, Y. Zhu, S. Xie, Z. Cheng, H. Che, Y. Shen, L. Chen, X. Huang, P. Pianetta, Z.-F. Ma, Y. Liu and L. Li, *Cell Rep. Phys. Sci.*, 2022, **3**, 100741.

20 S. Lei, W. Sun and Y. Yang, *Environ. Sci. Technol.*, 2024, **58**, 3609–3628.
21 G. Ji, J. Wang, Z. Liang, K. Jia, J. Ma, Z. Zhuang, G. Zhou and H.-M. Cheng, *Nat. Commun.*, 2023, **14**, 584.
22 Z. Zeng, P. Xu, J. Li, C. Yi, W. Zhao, W. Sun, X. Ji, Y. Yang and P. Ge, *Adv. Funct. Mater.*, 2024, **34**, 2308671.
23 X.-T. Wang, Y. Yang, J.-Z. Guo, Z.-Y. Gu, E. H. Ang, Z.-H. Sun, W.-H. Li, H.-J. Liang and X.-L. Wu, *J. Mater. Sci. Technol.*, 2022, **102**, 72–79.
24 L. Yang, W. Deng, W. Xu, Y. Tian, A. Wang, B. Wang, G. Zou, H. Hou, W. Deng and X. Ji, *J. Mater. Chem. A*, 2021, **9**, 14214–14232.
25 Y. Sun, S. Oh, H. Park and B. Scrosati, *Adv. Mater.*, 2011, **23**, 5050–5054.
26 H. Wang, Y. Yang, Y. Liang, L.-F. Cui, H. S. Casalongue, Y. Li, G. Hong, Y. Cui and H. Dai, *Angew. Chem., Int. Ed.*, 2011, **50**, 7364–7368.
27 Y. Deng, C. Yang, K. Zou, X. Qin, Z. Zhao and G. Chen, *Adv. Energy Mater.*, 2017, **7**, 1601958.
28 X. Cui, K. Tuo, H. Dong, X. Fu, S. Wang, N. Zhang, L. Mao and S. Li, *J. Alloys Compd.*, 2021, **885**, 160946.
29 I. M. Nwachukwu, A. C. Nwanya, A. B. C. Ekwealor and F. I. Ezema, *J. Energy Storage*, 2022, **54**, 105248.
30 Z. Zeng, H. Lei, C. Zhu, Y. Wen, X. Chen, S. Xu, W. Sun, P. Ge and Y. Yang, *Angew. Chem., Int. Ed.*, 2026, e7687036.
31 J. Liu, Y. Wu, B. Zhang, X. Xiao, Q. Hu, Q. Han, L. Wang, F. Bei and X. He, *Small*, 2024, **20**, 2309629.
32 S. Wi, J. Park, S. Lee, J. Kim, B. Gil, A. J. Yun, Y.-E. Sung, B. Park and C. Kim, *Nano Energy*, 2017, **39**, 371–379.
33 L. Wang, Y. Li, J. Wu, F. Liang, K. Zhang, R. Xu, H. Wan, Y. Dai and Y. Yao, *J. Alloys Compd.*, 2020, **839**, 155653.
34 S. Li, H. Zhang, Y. Liu, L. Wang and X. He, *Adv. Funct. Mater.*, 2024, **34**, 2310057.
35 D.-H. Baek, J.-K. Kim, Y.-J. Shin, G. S. Chauhan, J.-H. Ahn and K.-W. Kim, *J. Power Sources*, 2009, **189**, 59–65.
36 G.-W. Liu, X.-J. Zhang, S. Gong, D.-P. Jiang, B.-X. Liu, R. Yang and S.-G. Lu, *Rare Met.*, 2022, **41**, 3142–3149.
37 M. Fan, Q. Meng, X. Chang, C. Gu, X. Meng, Y. Yin, H. Li, L. Wan and Y. Guo, *Adv. Energy Mater.*, 2022, **12**, 2103630.
38 H. Yang, C. Fu, Y. Sun, L. Wang and T. Liu, *Carbon*, 2020, **158**, 102–109.
39 Y. Yang, M. Sun, W. Yu, X. Ma, S. Lei, W. Sun, S. Song and W. Hu, *Sustain. Mater. Technol.*, 2023, **36**, e00625.
40 X. Wang, Z. Feng, X. Hou, L. Liu, M. He, X. He, J. Huang and Z. Wen, *Chem. Eng. J.*, 2020, **379**, 122371.
41 X. Yan, D. Sun, Y. Wang, Z. Zhang, W. Yan, J. Jiang, F. Ma, J. Liu, Y. Jin and K. Kanamura, *ACS Sustainable Chem. Eng.*, 2017, **5**, 4637–4644.
42 J. Zhou, C. Xing, J. Huang, Y. Zhang, G. Li, L. Chen, S. Tao, Z. Yang, G. Wang and L. Fei, *Adv. Energy Mater.*, 2024, **14**, 2470033.
43 J.-K. Kim, R. Vijaya, L. Zhu and Y. Kim, *J. Power Sources*, 2015, **275**, 106–110.
44 Y. Liu, Y. Gu, H. Zeng, J. Zheng and F. Pan, *J. Phys. Chem. C*, 2019, **123**, 17002–17009.
45 C. Luo, Y. Jiang, X. Zhang, C. Ouyang, X. Niu and L. Wang, *J. Energy Chem.*, 2022, **68**, 206–212.
46 S. Pleuksachat, P. Krabao, S. Pongha, V. Harnchana, P. Klangtakai, W. Limphirat, S. Soontaranon, J. Nash and N. Meethong, *J. Energy Chem.*, 2022, **71**, 452–459.
47 J. Yang, C. Li, T. Guang, H. Zhang, Z. Li, B. Fan, Y. Ma, K. Zhu and X. Wang, *Nano Lett.*, 2021, **21**, 5091–5097.
48 D. B. Ravnsbæk, K. Xiang, W. Xing, O. J. Borkiewicz, K. M. Wiaderek, P. Gionet, K. W. Chapman, P. J. Chupas and Y.-M. Chiang, *Nano Lett.*, 2014, **14**, 1484–1491.
49 C. V. Ramana, A. Mauger, F. Gendron, C. M. Julien and K. Zaghib, *J. Power Sources*, 2009, **187**, 555–564.
50 T.-F. Yi, P.-P. Peng, Z. Fang, Y.-R. Zhu, Y. Xie and S. Luo, *Composites, Part B*, 2019, **175**, 107067.
51 X. Zhang, M. Hou, A. G. Tamirate, H. Zhu, C. Wang and Y. Xia, *J. Power Sources*, 2020, **448**, 227438.
52 Z. Chen, W. Wang, J. Duan, F. Qian, Y. Cao, J. He, D. Wang, P. Dong and Y. Zhang, *Ceram. Int.*, 2023, **49**, 18483–18490.
53 H. Shi, Y. Zhang, P. Dong, X. Huang, J. He, J. Duan, D. Wang and Y. Zhang, *Ceram. Int.*, 2020, **46**, 11698–11704.
54 W. Liu, P. Gao, Y. Mi, J. Chen, H. Zhou and X. Zhang, *J. Mater. Chem. A*, 2013, **1**, 2411–2417.
55 Y.-J. Zhong, J.-T. Li, Z.-G. Wu, X.-D. Guo, B.-H. Zhong and S.-G. Sun, *J. Power Sources*, 2013, **234**, 217–222.
56 B. Zhang, W. Meng, Y. Gong, G. Hu, Z. Peng, K. Du, B. Makuza, J. Wu, X. Xie and Y. Cao, *Mater. Today Energy*, 2022, **30**, 101162.
57 Z.-X. Chi, W. Zhang, X.-S. Wang, F.-Q. Cheng, J.-T. Chen, A.-M. Cao and L.-J. Wan, *J. Mater. Chem. A*, 2014, **2**, 17359–17365.
58 S. R. Das, S. B. Majumder and R. S. Katiyar, *J. Power Sources*, 2005, **139**, 261–268.
59 M. Wang, H. Liang, C. Wang, A. Wang, Y. Song, J. Wang, B. Wang, Y. Wei, X. He and Y. Yang, *Adv. Mater.*, 2023, **35**, 2306683.
60 Y. Wen, Z. Zeng, J. Li, Z. Dong, C. Zhu, H. Lei, P. Ge and Y. Yang, *Angew. Chem., Int. Ed.*, 2026, **65**, e8828799.